Chapter – 6

Compositional effect on solar-driven hydrogen evolution reaction in $\mathrm{Cu_{1-x}Ni_xO}$

Publication: *Ashish K. Ranjan, P. Singh, "Compositional effect on Solar-Driven Hydrogen Evolution Reaction in $Cu_{1-x}Ni_xO$". (To be communicated)*

CHAPTER 6: Compositional effect on solar-driven hydrogen evolution reaction in $\mathbf{Cu_{1-x}Ni_xO}$.

6.1 Introduction

In the previous chapter, it was discussed that the CuO nanoparticles synthesized by the Hydrothermal method were found to be structurally and thermally stable at room temperature. An impressive HER photocurrent density of -41.57 mA/cm^2 at -0.6 V vs RHE was obtained. This may be due to nanostructuring, which provides a more active site for the reaction. This shows that CuO is a promising material for HER. The bandgap of ~ 1.37 eV is greater than the theoretical potential (1.23 eV) of water splitting, making it a suitable photocathode material. However, due to the low bandgap, the chances of charge carrier recombination are apparent, and this directly affects the photoelectrochemical properties of the sample.

On the other hand, due to the lower bandgap, the electrons need less energy for transition to the conduction band. There are several methods to enhance HER activity or hydrogen production, such as nanostructuring [294][295][296], surface modification [297][298], doping [299][300], and surface engineering [301][302]. The present chapter discusses the effect of composition on the photoelectrochemical hydrogen evolution reaction.

6.2 Experimental Procedure

For the synthesis of $\mathrm{Cu_{1-x}Ni_xO}$ $(\mathrm{x} = 0, 0.2, 0.4, 0.6, 0.8, 1)$, CuO (bought from Merck), and NiO (bought from Alfa Aesar) with high purity (> 99%) were used as raw materials and were weighed according to the concentration in stoichiometric amount to obtain the desired composition. The solid-state reaction (SSR) method was utilized to synthesize the samples. The precursors were wet ground in the agate mortar and pestle in acetone for 2 hours. The obtained samples were calcined at 500°C for 1 hour. Then, the samples were pelletized using a hydraulic press with a pressure of 5 tons. All the samples were then sintered at 700°C for 2 hours with a heating gradient of 5°C/min. These samples were coded as N0, N2, N4, N6, N8, and N10 for x doping percentages of 0, 0.2, 0.4, 0.6, 0.8, and 1.0, respectively.

6.3 Characterization Techniques

XRD measurements were performed using Rigaku Miniflex II (Japan) with Cu-kα radiation (λ = 1.5406 Å). TGA/DSC measurements were performed in a nitrogen environment using Mettler Toledo, Germany, ranging from room temperature to 1000 °C. The surface morphology of all the samples was analyzed using HR-SEM (Nova Nano SEM, FEI). The ultraviolet photoelectron microscopy (UPS) measurements were performed using the K-Alpha model (Thermo Fisher Scientific). In photoelectrochemical measurements, linear sweep voltammetry, cyclic voltammetry, and chronoamperometry measurements were performed using a three-electrode setup, and the data was recorded using a Keithley 2450 source meter. The setup consists of an Ag/AgCl reference electrode, a Pt wire as a counter electrode, and a working electrode (sample to be measured). After that, the setup was immersed in an environment-friendly 1 M Na_2SO_4 electrolyte solution. The cyclic voltammograms were recorded at 25, 50, 100, and 150 mV/s scan rates, respectively. A solar simulator (Sciencetech, AM1.5 Global, class AAA) of Xenon Arc lamp having a power of 100mW/cm^2 was used as a light source.

6.4 Results and Discussion

6.4.1 Structural Studies

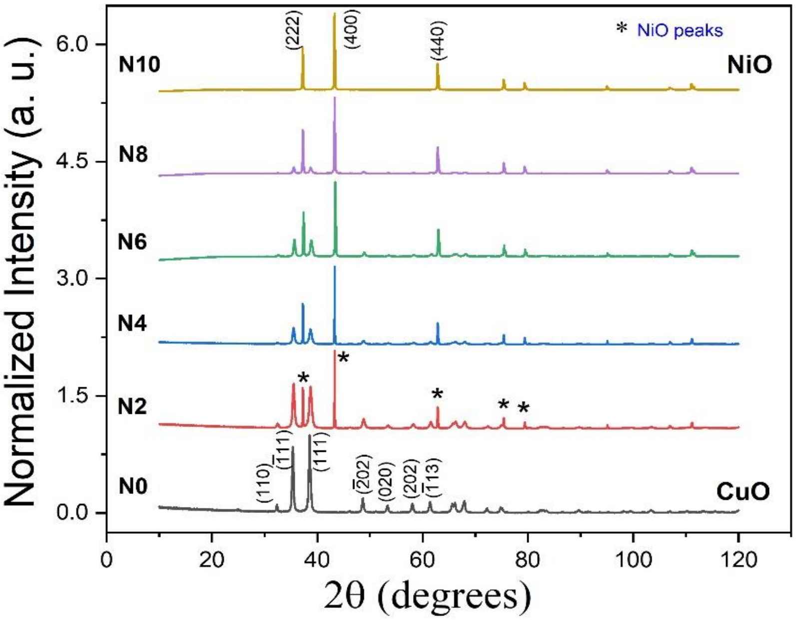

Fig. 6.1: Depicts the XRD of $Cu_{1-x}Ni_xO$ $(x = 0, 0.2, 0.4, 0.6, 0.8, 1)$ where N0, N2, N4, N6, and N8 show the formation of the composite.

Fig. 6.1 XRD patterns of the samples $Cu_{1-x}Ni_xO$ $(x = 0, 0.2, 0.4, 0.6, 0.8, 1)$ was recorded at room temperature in the 2θ range of 0 to 120 °C. CuO and NiO are known to have monoclinic structure with C2/c (HM #15) symmetry and cubic structure with $Fm\bar{3}m$ (HM #225) symmetry, respectively. The major diffraction peaks of CuO correspond to 32.21°, 35.24°, 38.50°, 48.60°, 53.14°, 57.91°, and 61.47° and can be indexed to (110), ($\bar{1}$11), (111), ($\bar{2}$02), (020), (202), and ($\bar{1}$13) planes, respectively, fit well with JCPDS card no. #89-5895. Similarly, the major diffraction peaks of NiO correspond to 36.99°, 43.3°, and 62.59° and can be indexed to (222), (400), and (440) planes, respectively, fitting well with JCPDS card no. #89-5881. Further, no other impurity peaks were observed.

6.4.2 Thermal study

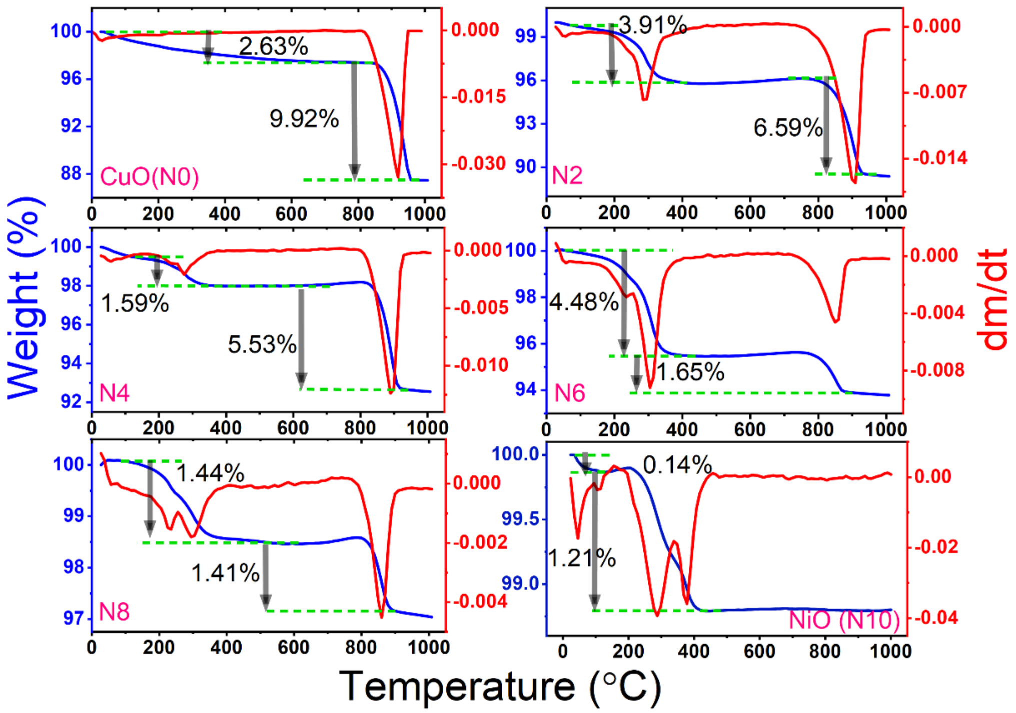

Figure 6.2: Depicts the mass loss and dm/dT variation with the temperature of all the calcined samples.

Fig. 6.2 shows the mass loss and dm/dT curve of N0, N2, N4, N6, N8, and N10 composites. It can be observed that there is a continuous two-step mass loss in all the samples. The initial step of mass loss occurs from 25 to 400 °C and corresponds to removing adsorbed water molecules on all the sample's surface. For the second step, in sample N0, a continuous mass loss at ~ 900 °C corresponds to the removal of organic components (OH groups) such as acetone. Similarly, in samples N2, N4, N6, and N8, beyond 400 °C to ~ 900 °C, and in sample N10, the mass loss at ~ 400 °C corresponds to the removal of organic components such as acetone. The first endothermic peak of the DSC curve in all the samples might represent the moisture removal corresponding to the initial mass loss step. At ~ 900 °C for the sample N2, N4, N6, and N8 and for N10 at ~ 400 °C, the second endothermic peak of DSC curves represents the melting process in the sample. The total mass loss corresponding to all the samples is tabulated in Table 6.1.

Table 6.1: Total calculated mass loss of pure and composite samples.

Sample name	Mass loss (%)
N0	12.55
N2	10.50
N4	7.12
N6	6.13
N8	2.58
N10	1.35

6.4.3 Microstructural study

The surface morphology of the $\mathrm{Cu_{1-x}Ni_xO}$ ($\mathrm{x} = 0, 0.2, 0.4, 0.6, 0.8, 1$) samples are analyzed using HR-SEM measurement. Fig. 6.3 shows the HR-SEM images of all the calcined samples. In sample N0, the grains formed are rectangular and quasi-spherical, while in samples N2, N4, N6, and N8, the grains are quasi-spherical. In sample N10, hexagonal-like grains are observed. Fig. 6.4 represents the grain size distribution plot of all the pure and composite samples. Further, the plot is fitted with Gaussian fitting to estimate the average grain size. The average grain size of N0, N2, N4, N6, N8, and N10 are tabulated in Table 6.2.

It is observed that the grain size of composite samples N2, N4, N6, and N8 are smaller compared to the pure samples. The reason behind the size alteration is the interaction between the different materials where nucleation and growth are affected. As a result, a reduced grain size is observed [303].

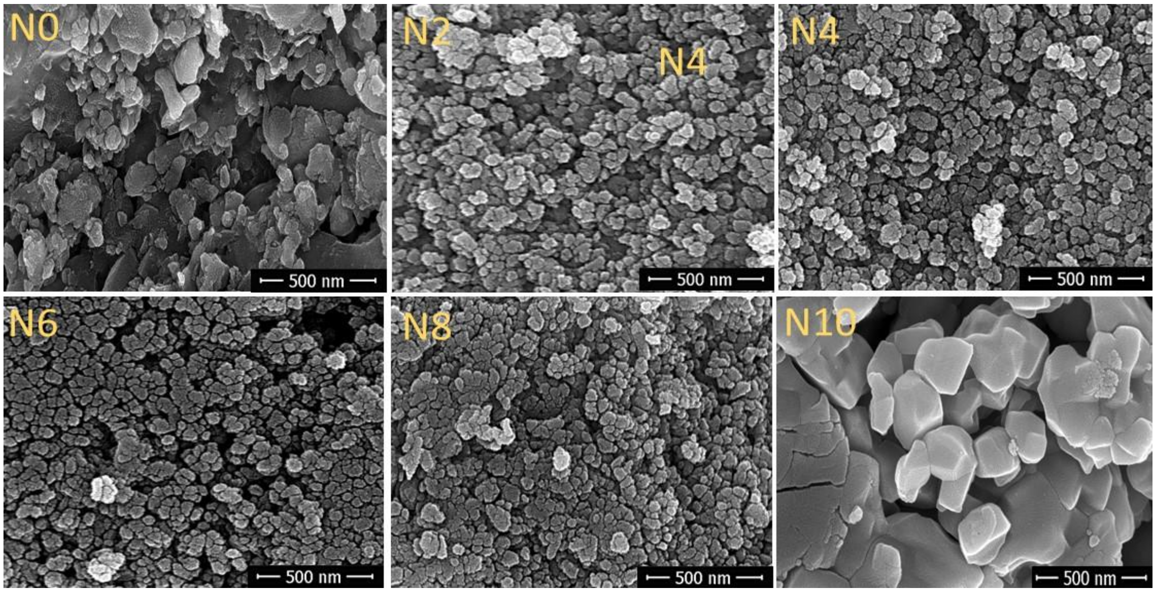

Figure 6.3: HR-SEM images of $Cu_{1-x}Ni_xO$ $(x = 0, 0.2, 0.4, 0.6, 0.8, 1)$ shows the calcined sample's rectangular, quasi-spherical, and hexagonal-like shape (in N10) at 500 nm resolution.

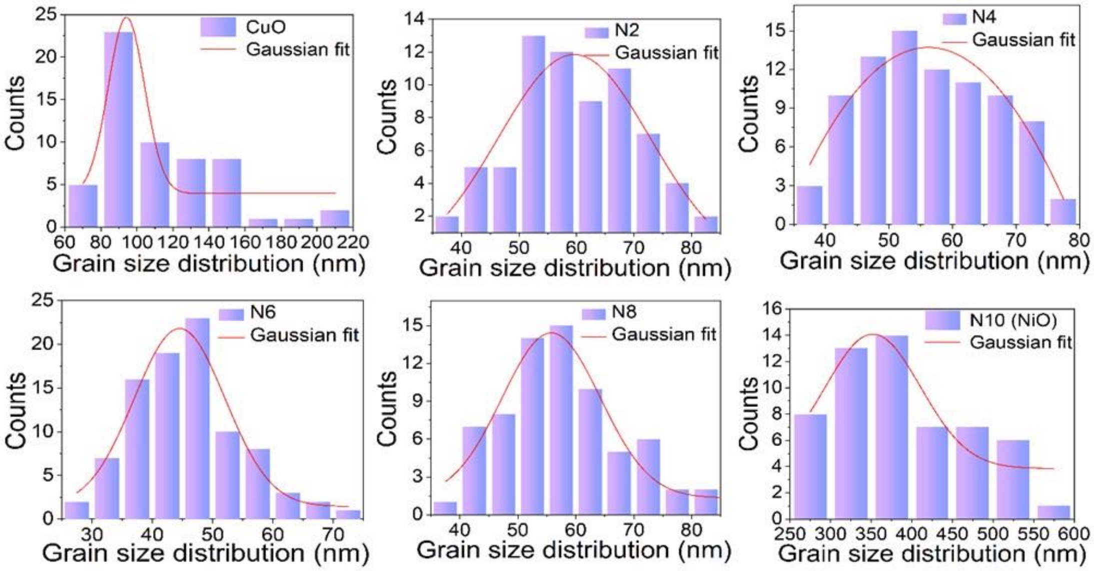

Figure 6.4: Depicts the grain size distribution images of $Cu_{1-x}Ni_xO$ $(x = 0, 0.2, 0.4, 0.6, 0.8, 1)$ and their fitting to estimate the average grain size.

Table 6.2: Grain size of calcined $\mathrm{Cu_{1-x}Ni_xO}$ $(x = 0, 0.2, 0.4, 0.6, 0.8, 1)$ samples.

Sample Name	Grain size (nm)
N0	94.20
N2	59.59
N4	56.21
N6	44.50
N8	55.75
N10	352.01

6.5 Photoelectrochemical study

To understand the photoelectrochemical behavior of $\mathrm{Cu_{1-x}Ni_xO}$ $(x = 0, 0.2, 0.4, 0.6, 0.8, 1)$, cyclic voltammetry was measured under the AM1.5 G solar light condition in the Na_2SO_4 electrolyte solution, as shown in Fig. 6.5. It was observed that the photocurrent density increases by increasing the scan rate (ν). Moreover, the peak current density (J_p) increases by increasing the doping concentration in N0 and N2. However, for the samples N4, N6, N8, and N10, the peak current density decreases by increasing the doping concentration. In sample N10, the OER peak is diminished, which shows that along with CuO, NiO is also a suitable catalyst for hydrogen production.

Further, the Randles – Sevcik (RS) equation shown in equation (2.5) was plotted to investigate the reversibility of all the samples, as shown in Fig. 6.6. In the RS equation, the peak current density is proportional to the square root of the scan rate ($J_p \propto \nu^{1/2}$). Therefore, the plots J_p vs

$\nu^{1/2}$ were linearly fitted, and the linear plots indicate the quasi-reversible nature of all the samples.

Further, to understand in-depth, the data was plotted on the log-log scale, and the slope was observed to be in the range of ~ 0.5 – 0.65, which indicates the quasi-reversible nature of all the samples.

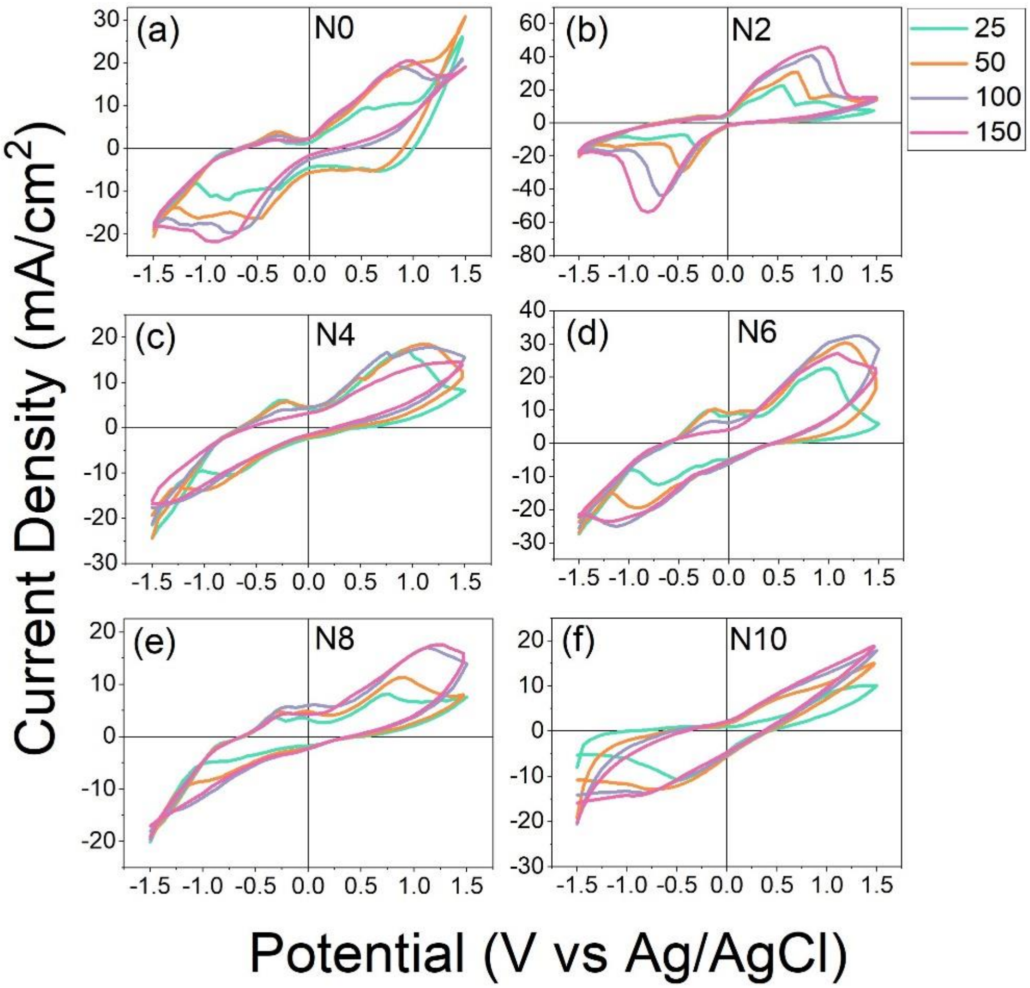

Figure 6.5: Represents the cyclic voltammogram of $\mathrm{Cu_{1-x}Ni_xO}$ ($x = 0, 0.2, 0.4, 0.6, 0.8, 1$) measured under solar light conditions at the scan rate of 25, 50, 100, and 150 mV/s.

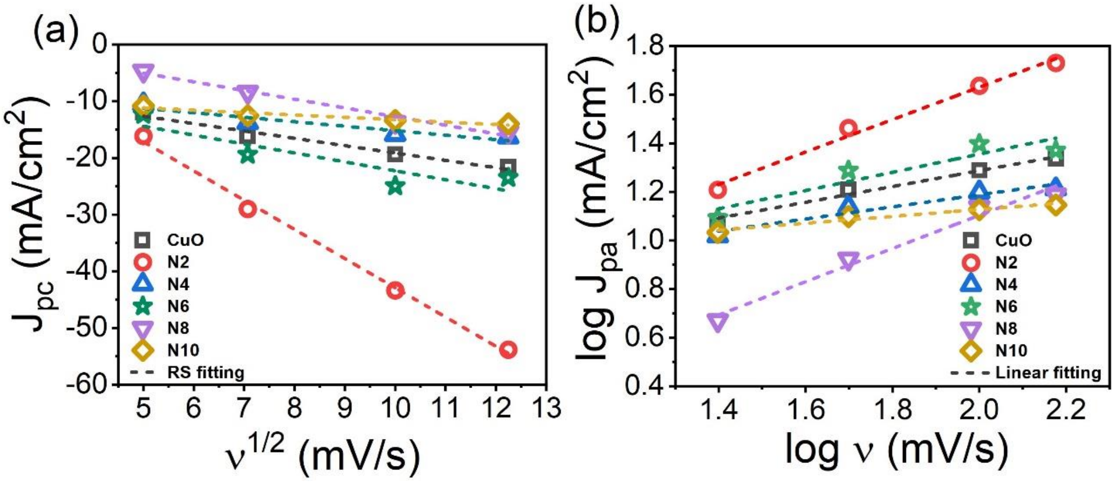

Figure 6.6: (a) Depicts the peak current density (J_p) vs $\nu^{1/2}$ and (b) log J_p vs log ν plot to understand the reversible nature of $Cu_{1-x}Ni_xO$ $(x = 0, 0.2, 0.4, 0.6, 0.8, 1)$.

6.5.1 Mott – Schottky plot analysis

To determine the semiconductor nature and potential required to avoid band bending, the Mott –Schottky (MS) plot was analyzed as shown in Fig. 6.7. The MS equation can be written as [304]:

$$\frac{1}{C^2} = \frac{2}{\varepsilon\varepsilon_0 A^2 e N_D}\left(V - V_{fb} - \frac{k_B T}{e}\right) \qquad (6.2)$$

Where C is interfacial capacitance, ε is permittivity, ε_0 is absolute permittivity, k_B is Boltzmann's constant, A is the area, T is absolute temperature, e is the electron charge, and V is the applied voltage.

The linear fitting of the MS plot affirms that all the samples exhibit p-type behaviour, and their x intercept indicates the flat band potential (V_{fb}). The V_{fb} obtained for N0, N2, N4, N6, N8, and N10 samples are 0.37, 0.36, 0.34, 0.62, 0.61, and 0.33 V vs Ag/AgCl, respectively.

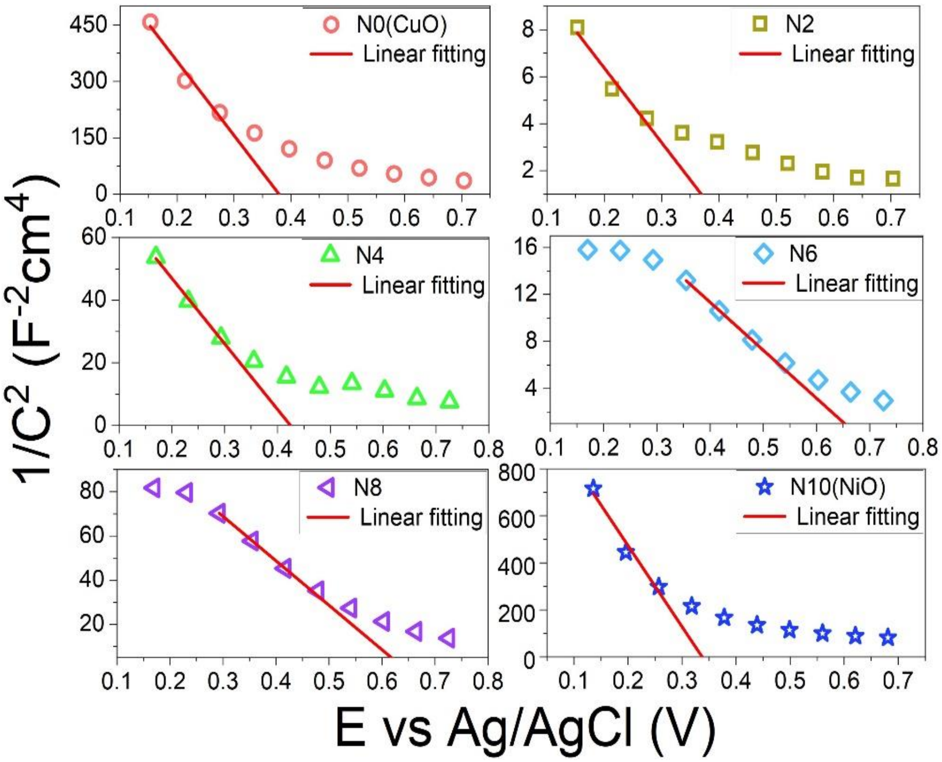

Figure 6.7: Depicts the Mott – Schottky plot of $Cu_{1-x}Ni_xO$ $(x = 0, 0.2, 0.4, 0.6, 0.8, 1)$ and their fitting to estimate the flat band potential.

6.5.2 HER Activity

An in-depth investigation was carried out to reveal the trend of HER activity of all the photocathodes in a neutral solution. The generally accepted mechanism for HER in neutral and alkaline media involves three elementary reaction steps [305][37]:

$$H_2O + e^- \rightleftarrows H_{ads} + OH^- \quad \text{(Volmer step)} \tag{6.3}$$

$$H_{ads} + H_2O + e^- \rightleftarrows H_2 + OH^- \quad \text{(Herovsky step)} \tag{6.4}$$

$$2H_{ads} \rightleftarrows H_2 \quad \text{(Tafel step)} \tag{6.5}$$

The initial (Volmer) step involves splitting water molecules and hydrogen adsorption on an unoccupied electrode/electrolyte interface site. After this, hydrogen is generated through either an electrochemical process (Heyrovsky step) or a chemical process (Tafel step).

Fig. 6.8 shows the LSV curves indicating HER photocurrent density (J) versus the potential (V vs RHE) plot of $\mathrm{Cu_{1-x}Ni_xO}$ $(x = 0, 0.2, 0.4, 0.6, 0.8, 1)$ under continuous light conditions. Interestingly, it was observed that sample N2 has an impressive HER photocurrent density of -42.64 mA/cm^2 at 0 V vs. RHE among all the photocathodes, suggesting better HER activity. This confirms that a very small doping concentration of NiO, i.e., x = 0.2, significantly enhances the HER activity.

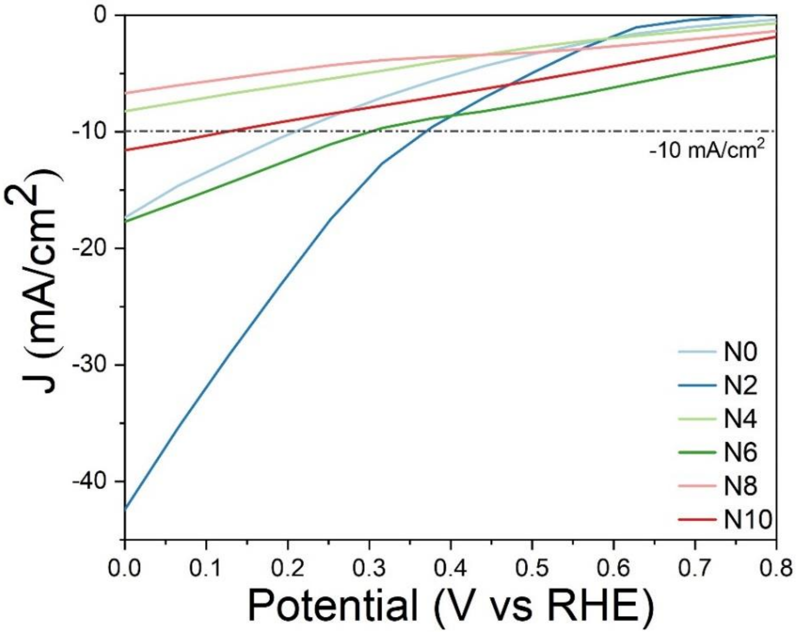

Figure 6.8: Linear sweep voltammetry of $\mathrm{Cu_{1-x}Ni_xO}$ $(x = 0, 0.2, 0.4, 0.6, 0.8, 1)$ consisting of onset potential, maximum photocurrent density at 0 V vs RHE, and overpotential at -10 mA/cm^2 for catalyzing HER.

However, the HER photocurrent density decreases while increasing the doping concentration, i.e., x = 0.4, 0.6, 0.8. Further, the onset potential values exhibited by N0, N2, N4, N6, N8, and N10 are 0.57, 0.58, 0.56, 0.58, 0.4, and 0.44 V (vs RHE) respectively. The N8 and N10 samples had the least onset potential due to the high concentration of NiO. Further, it was also observed that only N0, N2, N6, and N10 samples reached the standard current density of -10 mA/cm^2, indicated by a dashed line in Fig. 6.8. But, a sharp increase in photocurrent density (almost double) in N2 indicates high HER activity compared to the other photocathodes.

6.6 Conclusion

The composite and pure samples were synthesized using a solid-state reaction process where NiO was used as a dopant in stoichiometric ratios. The XRD results confirm the composite sample's formation with a monoclinic phase with C2/c symmetry and cubic phases with $Fm\bar{3}m$ symmetry for CuO and NiO, respectively. The TGA analysis reveals a maximum of 12.55% of mass is observed in N0 (CuO). After increasing the doping concentration of NiO, a significant decrease in mass loss is observed, suggesting that the samples are thermally stable. The HR-SEM images reveal that the grain size of composite samples N2, N4, N6, and N8 are smaller than the pure samples due to the interaction between different materials (CuO and NiO) affecting nucleation and growth. In the photoelectrochemical study, a maximum HER photocurrent density of -42.64 mA/cm^2 at 0 V vs. RHE is observed, suggesting high HER activity in the N2 sample. This study provides strategies to boost the HER activity of CuO-based photocathodes for solar hydrogen production.